Bulletin of Engineering Geology and the Environment (2024) 83:316
https://doi.org/10.1007/s10064-024-03809-4

ORIGINAL PAPER

The water weakening effect on the progressive slope failure under excavation and rainfall conditions

Xiang Yu[1,2] · Tao Zhao[2] · Bin Gong[2] · Chun'an Tang[1]

Received: 29 July 2023 / Accepted: 2 July 2024

Abstract

The water weakening effect refers to the gradual deterioration of soil mechanical properties under long-term saturation. This paper analyzed the impact of water weakening on slope stability under alternating excavation and rainfall. The field investigation speculated shale hydration as the cause of overall slope instability. The mechanical parameters of hydrated shale were determined by the parameter inversion and empirical estimation methods. The simulations were used to restore the process of parameter weakening and slope failure, and confirmed the fact that hydration causes landslide. Furthermore, the failure mechanism of slope and support structure under hydration were investigated. The results show that the mechanical parameters of the slope decreased linearly, whereas the plastic strain–time and total displacement-maximum shear stress curves of the hydrated shale exhibited three stages: slow initial growth, rapid growth in the middle term, and rapid increase in the later period; the rate of slope deformation and the factor of safety reduction also gradually increase over time; under middle stage of hydration, the middle to rear of shale were extruded, while the front first underwent tensile shear deformation, forming a plastic zone of at rear and front excavated slope; In the late stage, hydrated shale quickly reaches its yield limit (maximum shear stress of 270 kPa), the middle and rear shale is damaged and compresses the front, causing it to transform from tensile shear to compressive shear failure. The plastic zone in the rear extends forward and connects with the front ones, forming an overall landslide. Besides, preventing deep landslides caused by hydration through waterproofing, drainage, protection, and support for excavated slopes has proven difficult. Therefore, it is necessary to redesign treatment schemes based on the characteristics of stress, strain, and seepage.

Keywords Slope failure · Water weakening effect · Progressive instability · Excavation · Rainfall

Introduction

Slope failure sometimes exhibits progressive characteristics. Initially, a local soil mass will be damaged and form a plastic zone, which will then pull or push the rest to expand the plastic zone, ultimately leading to slope instability (Bastian et al. 2021; Gong et al. 2017; Yu et al. 2021). Landslide development often results from continuous exposure to a single factor, such as rainfall or excavation, or from the sequential impact of multiple inducing factors, including earthquakes and rainfall. Over the past few decades, the instability of engineering slopes caused by excavation and rainfall is countless, for example the improper excavation and rainfall-induced softening of weak interlayers led to a gently inclined bedding landslide at a construction site in Bijie City, Guizhou Province, China, resulting in 14 deaths and three injuries on January 3, 2022 (Tao et al. 2022). Similarly, sustained heavy rainfall triggered slope instability at an excavated cutting slope along the Mawlamyine Highway in Mon State, Myanmar, causing 75 deaths and 27 damaged buildings on August 9, 2019 (Panday et al. 2021). On September 2, 2018, both rainfall and excavation decreased the effective stress and tensile resistance of soil at the slope toe, damaging the northern slope of Mengdong Town, Yunnan Province, China, leading to 10 deaths and 11 missing persons (Yang et al. 2020a). On September 23, 2017, due to rainfall infiltrating along the cracks formed by excavation and weakening the mechanical parameters of the rock mass, a landslide occurred at the construction site of Sanli

✉ Bin Gong
bin.gong@brunel.ac.uk

[1] State Key Laboratory of Coastal and Offshore Engineering, Dalian University of Technology, Dalian 116024, China

[2] Department of Civil and Environmental Engineering, Brunel University London, London UB8 3PH, UK

Published online: 17 July 2024

Road in Libo County, Guizhou Province, China, resulting in 3 deaths and 6 injuries. The landslide blocked the highway ramp (Zhao et al. 2019). On August 27, 2014, a high-speed landslide occurred in Fuquan, Guizhou, China, 23 people were killed, 22 were injured, and 77 houses were damaged. On site research shows that excavation leads to stress concentration at the middle of the slope, and subsequent rainfall causes an increase in groundwater level, both of which jointly trigger landslides (Lin et al. 2018a, b). These cases illustrate that slope failure resulting from combined excavation and rainfall has become a significant engineering problem, not only resulting in substantial economic losses but also posing a serious threat to civilian safety.

Currently, significant research has been conducted on the mechanism of shallow progressive landslide caused by excavation and rainfall. Scholars have found that excavation unloading can cause stress field adjustment, leading to excessive differences between major and minor principal stresses of rock and soil mass, which in turn leads to crack expansion and generation due to shear stress exceeding peak strength (Fang et al. 2022a; Feng et al. 2022; Liang et al. 2014; Wang et al. 2022; Xu et al. 2023; Yang et al. 2023). Meanwhile, excavation can result in loss of slope effective mechanical support, as well as providing an infiltration channel for rainfall (Gong 2021; Li et al. 2020a; Peng et al. 2019; Robert 2017; Shi et al. 2021). Subsequent rainfall reduces matric suction and effective stress of unsaturated soils (Fredlund and Lim 1994; Oh and Lu 2015; Bishop 1959), decreasing shear strength parameters while increasing the density of rock and soil mass (Qi et al. 2022; He et al. 2022). Rainfall promotes crack development, drive the sliding surface to expand with the formation of new plastic zone, and rapidly transform local deformation into a landslide. Infiltration along the excavated slope surface erodes the slope toe, causing failure and tractive landslides. Simultaneously, the accumulation at the slope crest cracks generates hydrostatic pressure, compressing the rock and soil mass at the rear and in turn resulting in a push-type landslide. However, the mechanism of deep landslides remains a complex topic. Several studies have shown that the sliding surface in engineering slopes with groundwater often coincides or intersects with the elevated water level replenished by rainfall (Zhang et al. 2021; Lin et al. 2018a, b). Additionally, the softening of sliding zone soil is significantly higher than that of saturated soil, indicating further reduction in mechanical parameters of rock and soil below the water level due to the hydration or water weakening effect (Meng et al. 2020; Zhu et al. 2020).

Experimental studies on various rock and soil masses under long-term saturation have shown that water causes minerals volumetric expansion, cement dissolution between particles, and microcracks expansion, leading to a decrease in compressive and tensile strength, elastic modulus, critical strain, and shear strength over time (Zhu et al. 2022; Zhao et al. 2022a, b; Chen et al. 2019a, b; Liu et al. 2022). Water weakening is being recognized as an important factor inducing disasters in deep soft rock formations to date, such as large deformation of tunnel surrounding rocks (Yang et al. 2020b; Bian et al. 2019) and the formation of weak intercalations in slopes (Huang and Gu. 2017; Zhang et al. 2017). Nevertheless, the study of the impact of hydration on slope stability and the mechanical behavior of engineering rock masses under hydration is still limited.

In this study, an engineering slope affected by excavation and rainfall was taken as an example. Firstly, through field investigation and geological survey, the shale hydration due to rainfall infiltration was identified as the primary factor contributing to overall slope instability. Secondly, the mechanical parameters of hydrated rock and soil mass were determined using the parameter inversion and formula calculation. Lastly, the numerical simulations were conducted to reveal the slope progressive failure process and mechanism, as well as the mechanical behavior of the engineering rock and soil mass under hydration.

Overview of the highway slope

Basic characteristics and failure process

The studied highway slope is situated in Guangdong Province, China. The slope is covered with dense vegetation, which can be divided into K158 + 280 ~ 590 and K158 + 590 ~ 700 sections by a gully, as depicted in Fig. 1(a). The terrain slopes downwards from north to south, with a relative height difference of 90 m, as shown in Fig. 1(b). The natural slope angle ranges from 16° to 20°, and the inclination is 180°. The area presents a syncline structure, the north and south rock strata dip between 15–53° and 19–61° respectively, which are both dip rock strata and not conducive to slope stability.

The K158 + 280 ~ 590 section, which was selected as the case slope, experienced progressive failure due to rainfall infiltration on the excavated slope surface. The initial excavation began in November 2015 and ended in April 2016, forming a three-level slope, each with a slope ratio of 1:1.1 and a height of 10 m. In early May of the same year, a continuous rainfall occurred, lasting for 93 days and resulting in an accumulation of 1992 mm. Following the rainfall, the excavated slope collapsed, 11 underground water springs were revealed at the lower first level slope to slope toe, as depicted in Fig. 2(b).

After the excavated slope failed, a modified construction plan was adopted, which included adjusting each level slope ratio to 1:1.25, wall masonry protection and 12 m full-length bonded bolt support. Meanwhile, ditches were

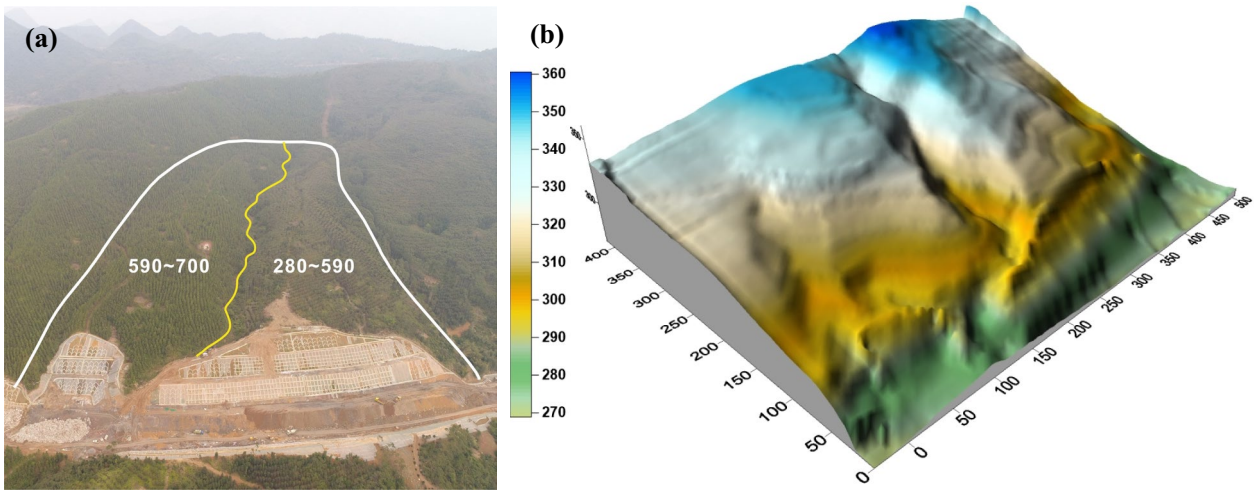

Fig.1 Slope topography and geomorphic characteristics: (**a**) UAV image, (**b**) 3D terrain map

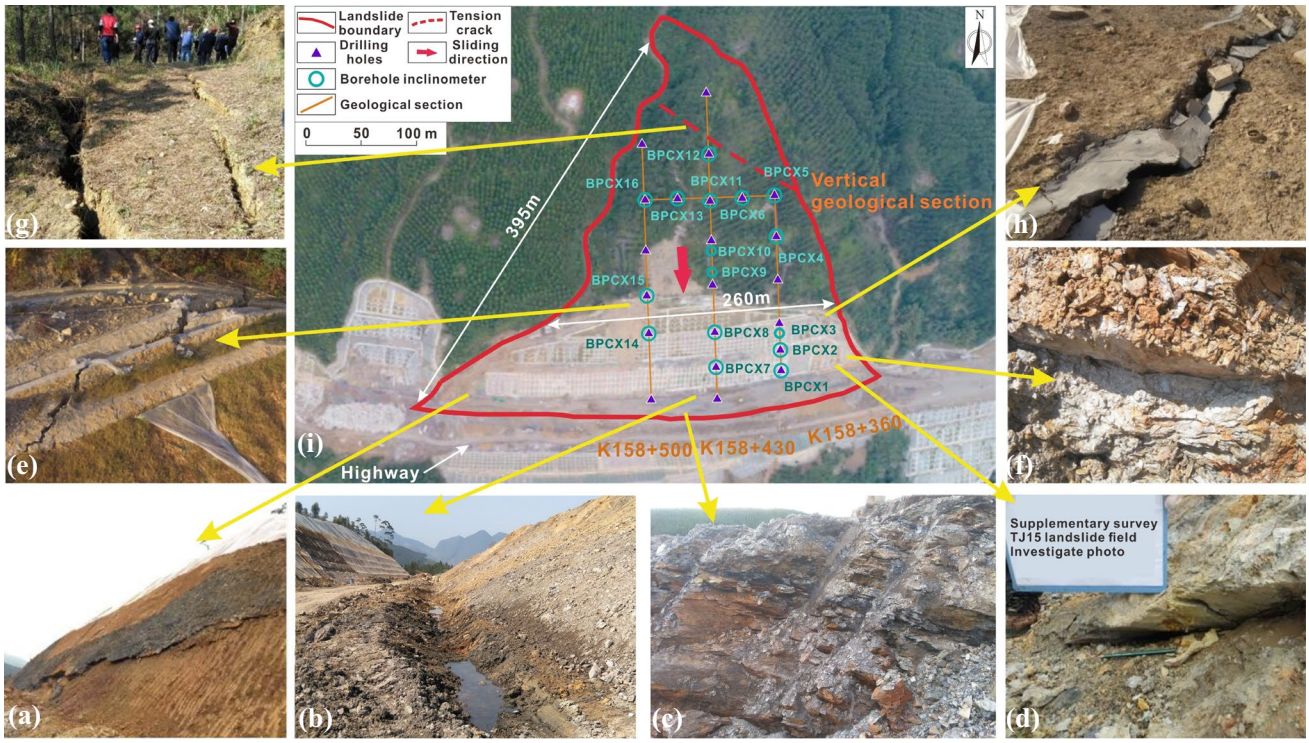

Fig.2 The landslide characteristics: (**a**), (**d**), (**f**) shear outlets, (**b**) underground water springs, (**c**) landslide drumlin, (**e**), (**h**) cracks, (**g**) through cracks, and (**i**) remote sensing image of landslide area

also set on the slope shoulder to intercept surface runoff. Unfortunately, the slope slid and significant deformed just 30 days after construction was completed. The front toe extruded and uplifted to form a landslide drumlin, as shown in Fig. 2(c). Shear outlets were found at the lower first level slope, as depicted in Fig. 2(a), (d), and (f). At the middle, soil masses from the first and second level slid, causing the first-level platform to stagger by 0.6 m. Cracks were also observed at the intercepting ditch of the slope shoulder and the second platform, as seen in Fig. 2(e) and (h), suggesting that the supporting structure wasn't effective. A large number of through cracks with a width of 50-100 cm were also observed 135–240 m behind

the slope shoulder, as shown in Fig. 2(g). The large-scale landslide from the top to the foot of the slope has formed.

Field investigation and analysis

After the landslide, geological survey and deformation monitoring were carried out on the slope area. To begin with, based on the location of tension cracks and landslide drumlin, it is estimated that the sliding direction is 178°. Next, to explore groundwater level and strata, a total of 22 geological boreholes were drilled along the sliding direction and route, forming three geological sections K158 + 360, 430, and 500, as well as one cross-section, as shown in Fig. 2(i). Furthermore, in order to determine the sliding surface, 16 monitoring holes (BPC1 ~ 14) were arranged in the geological borehole and its vicinity, and the inclinometer is used to measure the movement of the sliding body, as shown in Fig. 3(a), (b) and (c).

The drilling results show that the strata are gently inclined from north to south and basically parallel to the terrain from east to west. The slope is covered by argillaceous sandstone, carbonaceous shale, and argillaceous limestone from top to bottom. The sandstone cores are broken and soft, showing no apparent signs of immersion, as depicted in Fig. 3(e). The shale cores are earthy and wet, displaying obvious slip marks, as illustrated in Fig. 3(f). The limestone cores are incomplete and hard, without sliding mark on the surface, as shown in Fig. 3(g). Groundwater levels were observed 32 times, including 16 times both for initial water and stable water level, all of which were located in the lower carbonaceous shale. Groundwater was found to be gushing out at the front of K158 + 430 section, with a daily inflow of 0.72 tons. The location is close to the water springs, indicating that the groundwater level has hardly changed after local failure, as shown in Figs.2 (b) and 3 (h). Combined with the preliminary investigation report, it can be speculated that the initial groundwater level is located at the upper argillaceous limestone and rises to the lower carbonaceous shale after being recharged by rainfall in May, 2016.

To initially determine the position of the sliding surface and monitor the further development of the landslide, a total of 16 deep displacement monitoring points were installed on the slope. Meanwhile, the inclinometers were utilized to track the changes of slope displacement. Deep displacement monitoring began on October 6th, 2016 after the landslide, and ended on November 28th. BPCX1-5 monitoring holes are arranged at K158 + 360 section. Based on the inflection point of the displacement curve, the sliding surfaces

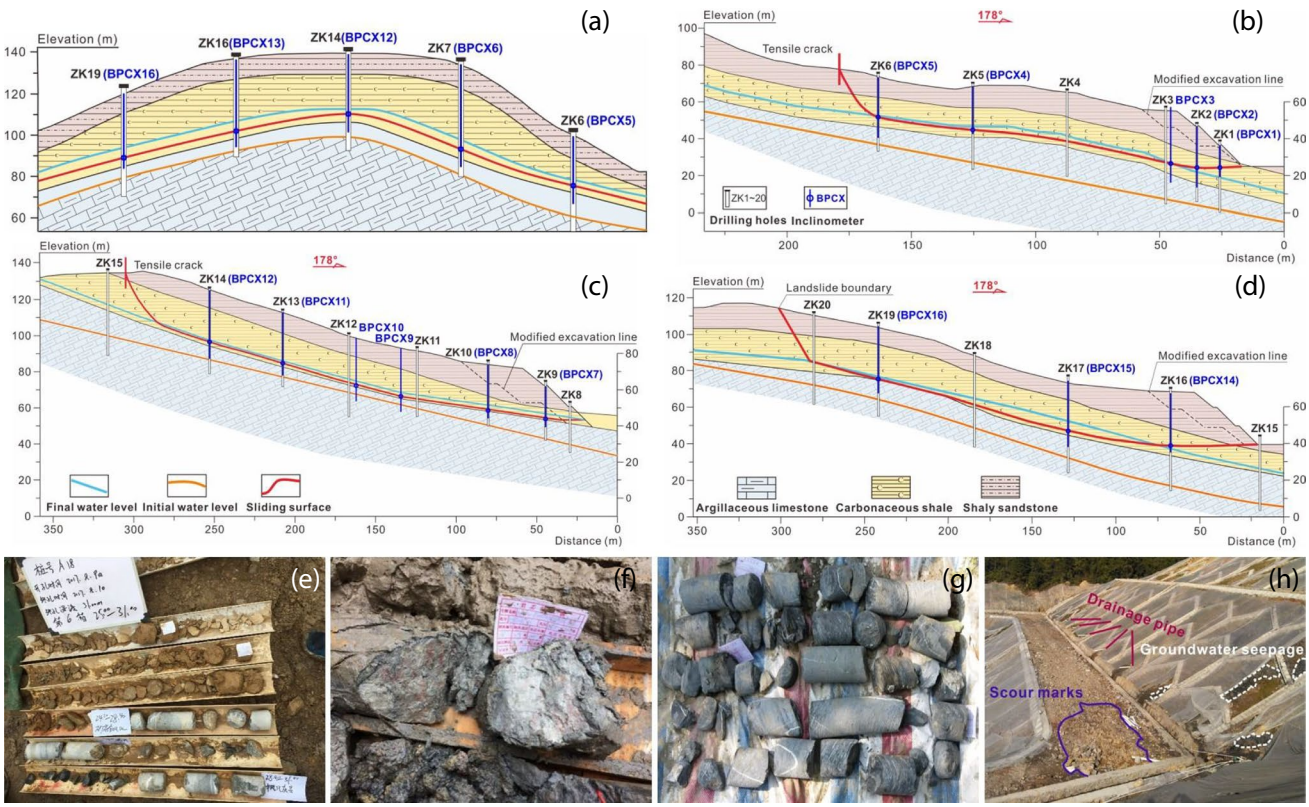

Fig.3 Field investigation: (**a**) the geological cross section, (**b**), (**c**), (**d**) K158 + 360, 430, and 500 sections (**e**), (**f**), (**g**) cores of argillaceous sandstone, carbonaceous shale and argillaceous limestone, and (**h**) groundwater seepage at lower first-level slope

is speculated at 12.2, 22.7, 28.6, 23.8, and 22 m below the surface, with cumulative displacement of 60.1, 57.4, 49.4, 18.3, and 24.2 mm. BPCX7-12 monitoring holes are set up at K158 + 430 section, the sliding surface is speculated at 18, 24.9, 26.7, 25.7, 28.3, and 28.9 m deep, with cumulative displacement of 64.4, 53.1, 22.6, 24.1, 37.6, and 41.2 mm. BPCX14-16 boreholes are arranged at K158 + 500 section, the sliding surface is speculated at 31.3, 26, and 30.1 m deep, with cumulative displacement of 43.5, 20.9, and 28 mm. BPCX6 and BPCX13 are arranged at the cross-section, the sliding surface is speculated at 29.7 and 28.2 m deep, with cumulative displacement of 35.7 and 31.5 mm.

Based on the displacement inflection point and the core data with sliding traces obtained from drilling exploration, the depth of sliding surface was completely determined, as shown in Fig. 3(a) ~ (d). The landslide type was a bedding landslide. The sliding surface rapidly extended downwards to the carbonaceous shale and cut out from the first level slope. This result is consistent with the obvious scratches on the carbonaceous shale core, manifesting that the sliding zone is the lower carbonaceous shale. Since the depth and cumulative deformation of the slip surface at the K158 + 430 section are the largest, and the landslide drum and tensile cracks are located nearby, it can be basically determined that this section is the main axis of the landslide. Considering that the lower shale is extremely soft and humid, water should be main induce factor. During the initial excavation stage, continuous rainfall causes the groundwater level to rise to the lower part of the carbonaceous shale and remain unchanged. Meanwhile, the modified excavated surface and slope top were covered with mortar rubble and vegetation, and no water flow was found in the gullies. These indicate that the slope is unlikely to be damaged due to consolidation or rainfall infiltration. Thus, it is highly likely that the landslide is due to the water weakening effect, which means that the strength of the sliding zone soil decreases and undergoes creep deformation under 30-days immersion. To verify this hypothesis, it is necessary to analyze the slope stability under hydration.

Parameters and Numerical configuration

To analyze the stability of slopes under hydration, it is imperative to study the influence of water on the mechanical parameters of shale first. Previous studies have suggested that prolonged immersion can result in erosion and dissolution of the cement between shale particles, leading to weakened cementation and decreased cohesive force of the rock mass (Wong et al. 2016; Ewy 2014; Jiang et al. 2014). Moreover, the hydration film on mineral surfaces becomes thicker, which lubricates the contact surface between particles and reduces its internal friction angle (Leng et al. 2022; Zhao et al. 2022a, b; Mao et al. 2010). Additionally, hydration can cause particle expansion and fall off, resulting in crack expansion, pore increase, and a reduction in the elastic modulus of shale (Bian et al. 2019; Li et al. 2020b; Chen et al. 2019a, b). Therefore, this study will first determine the shear strength and elastic modulus when overall landslide occurred. Namely, after 30 days of hydration, and then restore the hydration process in the finite element simulation by setting the parametric weakening function.

Inversion of shear strength parameters

Due to differences in mineral composition, weathering degree, and structure, the shear strength parameters of hydrated shale vary greatly. To eliminate this variability, parameter inversion is conducted using Geo-studio software based on the limit equilibrium method (Nguyen 1984; Ishii et al. 2012; Shinoda et al. 2019). This involves continuously reducing the cohesive force and internal friction angle according to a certain proportion until the slope factor of safety falls within the target.

Since landslide characteristics have already formed without significant mass movement, it can be basically determined that the slope slightly breaks the limit equilibrium state ($FoS \leq 1$) and has not yet entered the stage of severe sliding (Wang et al. 2017). Considering the result obtained from two-dimensional analysis is conservative due to the soil arching effect (Liu et al. 2021), the target safety factor for parameter inversion is set to 1, and the inversion is conducted on the sliding surfaces of K158 + 360, 430, and 500 sections after modified excavation. The excavated slope is reinforced by 12 m full-length bonded anchor rods with a design bond strength, the bearing and shear bearing capacity of 360 kPa, 300 kN and 240 kN, respectively.

Referring to the experimental research (Yang et al. 2021; Zhu et al. 2019a, b; Kang 2019; Wang 2015), the cohesion and internal friction angle of carbonaceous shale below the water level will be reduced in a ratio of 1:2. The saturation parameters will be selected as the initial values, and the rest rock and soil mass still used natural parameters. When one of the three sections reaches the safety factor of 1 through reverse calculation, the reduced shear strength parameters are the hydrated parameters. It is worth noting that the shear strength parameters obtained through parameter inversion are not only used to calculate the safety factor but also considered as the actual material properties of the hydrated rock and soil mass. Table 1 shows the physical and mechanical parameters, with the parameters in parentheses representing the saturation parameters obtained from geotechnical tests.

The inverted parameters are presented in Table 2. When the cohesive force and internal friction angle of the weakened carbonaceous shale are 15 kPa and 15°, the critical factor of safety for the K158 + 360, 430 and 500 section are

Table 1 Physical and mechanical parameters of the geomaterials

Formation	Elastic modulus (kPa)	Poisson's ratio	Weight (kN/m^3)	Cohesive force C (kPa)	Internal friction angle φ(°)
Shaly sandstone	1.5×10^5	0.31	21	29.4	19
Carbonaceous shale	6.1×10^5 (5.7×10^5)	0.27	22 (23.5)	37 (31)	24 (23)
Argillaceous limestone	8.3×10^5 (7.6×10^5)	0.29	23.5 (24)	80 (76)	31 (29)

Table 2 Parameter inversion of water-weakened carbonaceous shale

Reduction ratio between C and φ	C (kPa)	φ (°)	Factor of safety of K158 + 360 section	Factor of safety of K158 + 430 section	Factor of safety of K158 + 500 section
Initial parameters	31	23	1.331	1.265	1.283
2:1	27	21	1.22	1.113	1.167
	23	19	1.113	1.054	1.094
	19	17	1.058	1.025	1.05
	15	15	1.007	0.998	1

1.007, 0.998 and 1, respectively, as shown in Fig. 4. Therefore, this set of cohesion and internal friction angle values are regarded as the water-weakened parameters of carbonaceous shale after 30 days of hydration.

Elastic modulus under hydration

Based on the mechanical tests of shale, the reduction rate of peak strength and elastic modulus is relatively similar within 30 days of immersion (Li et al. 2020a, b). The ratio of strength and modulus of immersed to dried shale can be used to indicate the water weakening effect on mechanical parameters (Chen et al. 2013):

$$\mathrm{K} = \frac{\sigma_w}{\sigma_c} = \frac{E_w}{E_c} \tag{1}$$

where K is softening coefficient, σ_w and E_w are the peak strength and elastic modulus of water immersed shale, respectively. σ_c and E_c are the peak strength and elastic modulus of dried shale, respectively. As the peak strength is commonly utilized to represent the shear strength, the elastic modulus of the immersed rock can be determined by multiplying the shear strength ratio of the immersed and dried shales with the elastic modulus of the dried rock:

$$E_w = \frac{\tau_w}{\tau_c} \times E_c \tag{2}$$

where τ_w and the τ_c is the shear strength of the immersed and dried shale, respectively. The shear strength parameters are based on the previous inversion results, c^w=15 kPa, φ^w =15°. The geological prospecting data provides the elastic modulus and shear strength parameters for the dried shale,

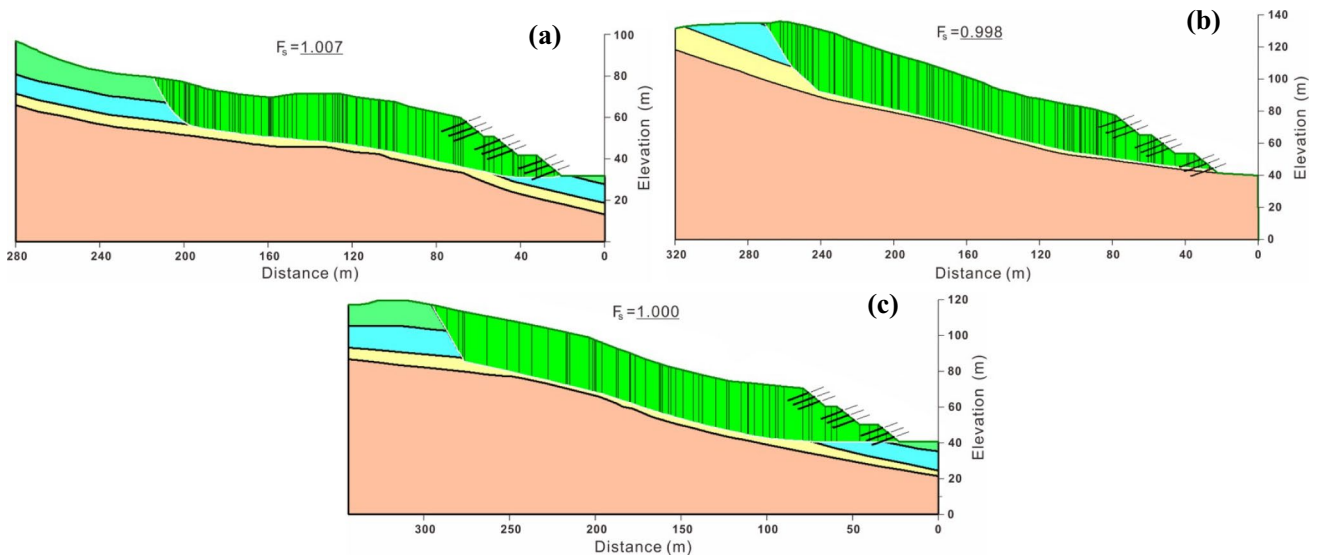

Fig.4 Final sliding surfaces of parameter inversion: (**a**) K158 + 360 section, (**b**) K158 + 430 section, and (**c**) K158 + 500 section

E_c=6.1 × 10^5 kPa, c = 37 kPa and φ=24°. Based on the Mohr–Coulomb strength theory, a soil element was considered in the hydrated carbonaceous shale as an object. It is assumed that the maximum principal stress σ_1 on the element is vertical while the minimum principal stress σ_3 is horizontal. As the argillaceous sandstone and carbonaceous shale above the underground water level are dry, the pore water can be disregarded under the weight of the thick overlying masses. When the unit shear failure occurs, the shear strength, maximum, and minimum principal stress can be expressed as follows:

$$\begin{cases} \sigma_1 = \gamma z \\ \sigma_3 = \sigma_1 \tan^2(45° - \frac{\sigma}{2}) - 2c\tan(45° - \frac{\varphi}{2}) \\ \tau = \frac{1}{2}(\sigma_1 - \sigma_3) sin2\alpha \end{cases} \quad (3)$$

where α is the included angle between the fracture surface and the direction of the maximum principal stress, $\alpha = 45° + \frac{\varphi}{2}$. The average thickness of the argillaceous sandstone and carbonaceous shale above the water level was initially estimated to calculate the maximum principal stress (477.17 kPa), using formula (3). Then, the strength parameters of the immersed and dried shale were introduced separately into formula (3), and the shear strength τ_w and τ_c were calculated in combination with the maximum principal stress. The shear strength τ_w=106.02 kPa, τ_c=147.98 kPa. Finally, the shear strengths and the elastic modulus of dried shale E_c were inserted into formula (2) to derive the elastic modulus of the immersed shale $E_w = 4.4 \times 10^5$ kPa. Compared with the elastic modulus of dried carbonaceous shale, the modulus of shale after 30 days of immersion decreased by 28.4%, which is similar to the modulus loss rate of 25.05% and 31.5% measured respectively by uniaxial and triaxial tests (Bian et al. 2019; Zhao et al. 2022a, b). Compared to short-term saturated carbonaceous shale, its elastic modulus decreases by 22.8%.

Numerical configuration

For the analysis of slope failure, this study utilized the stress-seepage-slope construction stage group in the two-dimensional finite element software Midas-GTX (MIDAS Information Technology Co., Ltd.), and the factor of safety was calculated using the strength reduction method. The numerical model was configured according to the landslide's main section (K158 + 430). The left and right boundaries were supported by vertical sliding bearings, while fixed bearings were applied to the bottom boundary. The model adopts quadrilateral elements with a total of 64,131 elements, the initial excavation and modified excavation + anchor rod support were completed in one construction stage each, the rainfall is simulated using a transient seepage module, and the flow boundary (21.42 mm/day) obtained by dividing the total rainfall by the duration is applied to the initial excavation slope and road, the initial groundwater level is set at argillaceous limestone.

The parameters of soil seepage characteristics include the unsaturated permeability coefficient and the soil–water characteristic curve (Fredlund 1998), the later was calculated using the Van Genuchten model (Parker et al. 1985) and combined with the saturated permeability coefficient to obtain the former. The V-G model parameters and saturated permeability coefficients listed in Table 3 were determined based on experimental studies of seepage in carbonaceous shale, argillaceous sandstone (Tong 2018; Moazeni-Noghondar et al. 2021), and argillaceous limestone (Xu et al. 2008; Wang 2012). As the rock masses below the initial water level were saturated throughout, its permeability characteristics were not considered. The governing equation for the V-G water content function model is as follows:

$$\theta_w = \theta_r + \frac{\theta_s - \theta r}{[1 + (\frac{\psi}{a})^n]^m} \quad (4)$$

where θ_w is the volumetric water content; θ_r is the residual volumetric water content; θ_s is the residual volumetric water content; ψ is the negative pore water pressure; a, n, and m are the curve fitting parameters.

The simulated conditions were set in the following order: in-situ stress balance → initial excavation → rainfall → modified excavation and support → hydration. At the end of the rainfall stage, the shear strength and elastic modulus of carbonaceous shale below the simulated saturation line (final groundwater level) were replaced with saturation parameters, as the initial values for subsequent hydration analysis. By subtracting the initial value from the parameters after 30th day of hydration and dividing by the duration, the daily decreases of cohesion, internal friction Angle and elastic modulus during hydration were

Table 3 The *VG* model parameters and saturated permeability coefficients

Types of rock and soil layers	a (kPa)	n	m	θ_r	θ_s	k_s (m/s)
Shaly sandstone	38.92	1.60	0.3742	0.054	0.275	7.16×10^{-4}
Carbonaceous shale	24.88	1.50	0.3316	0.12	0.326	5.48×10^{-5}
Argillaceous limestone	12.82	3.39	0.7050	0.218	0.323	1.12×10^{-5}

0.53 kPa, 0.27° and 4,333 kPa, respectively. Based on the above data, construct parameter weakening functions with an independent variable of 30 days, integrate it into saturated carbonaceous shale material, and activate it in the final construction stage. Then, the stability of the slope under hydration can be analyzed.

Result and Analyses

The following study employs numerical calculations to analyze and discuss simulation results. Specifically, the slope stability and deformation characteristics were presented and analyzed in the first and second chapter. The third chapter focuses on analyzing the mechanical behaviors of carbonaceous shale under hydration, using curves of plastic strain over time, maximum shear stress versus displacement, maximum shear stress over time, and major principal stress over time. In the fourth part, the failure mechanism of slope and the existing supports are studied, as well as the improved support scheme is proposed.

Slope deformation process and stability

Considering the large number of time steps involved in the analysis of hydration, representative simulation results for the 10th (initial), 20th (middle), and 30th days (late) are displayed alongside the results of two excavation and rainfall conditions. Figure 5 presents the effective plastic strain evolution. Over the course of construction, the scope of slope failure shifted from shallow to deep, while the failure type transitioned from local collapse to overall bedding sliding. Following initial excavation, a plastic zone developed along the excavated slope, with its maximum value located at the slope toe. During the rainfall stage, the plastic strain extended from the toe to the upper excavated slope, indicating a traction landslide pattern. Additionally, a new plastic zone formed in the middle of the slope, extending towards the slope top and originating from the saturated shale.

After modifying the excavation and implementing slope support, the plastic strain at the middle and rear of the slope disappeared, while a shallow plastic zone appeared from the slope toe to the second-level slope. However, carbonaceous shale hydration caused the slope to deform and slide once again. By the 10th day of hydration, the shallow plastic zone had transformed into a deep-seated sliding surface that circumvented the support structure and cut along the hydration layer. Simultaneously, the plastic zone from the hydration layer in the middle extended towards the slope top. On the 20th day of hydration, both the front and rear plastic zones expanded; the front plastic strain increased significantly, and the rear plastic zone began extending downward along the weakened shale, with a tendency to connect to the front sliding surface. By the 30th day of hydration, the front and rear plastic zones had fully connected, forming a large landslide mass that spanned the slope from top to toe.

Figure 6 displays the variation of the slope factor of safety during each modeling stage. During the construction stage, slope stability initially decreased rapidly, followed

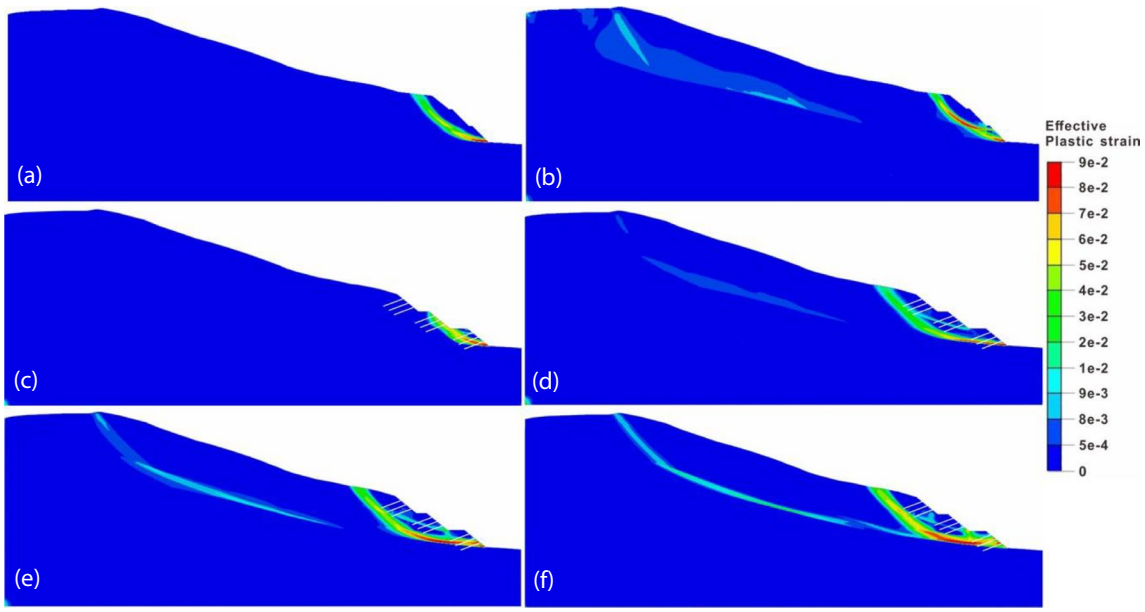

Fig.5 Evolution process of slope plastic strain under different analysis condition: (**a**) initial excavation (**b**) rainfall (**c**) modified excavation and support (**d**), (**e**) and (**f**) represent 10, 20 and 30 days of hydration

by a brief increase and subsequent decrease. After 30 days of hydration, the slope factor of safety reached 0.996, and was close to the slope factor of safety 0.998 obtained from parameter back analysis. This indicates good consistency between numerical simulation and inversion. According to Wang et al. (2017), who summarized the relationship between deformation and factors of safety, the cutting slopes can be categorized into the creeping stage ($1.05 < FoS < 1.1$), the extrusion stage ($1.02 < FoS < 1.05$), the sliding stage ($0.98 < FoS < 1.02$), and the sudden slip stage ($0.95 < FoS < 0.98$), the following section presents an analysis of the slope failure characteristics based on the four stages.

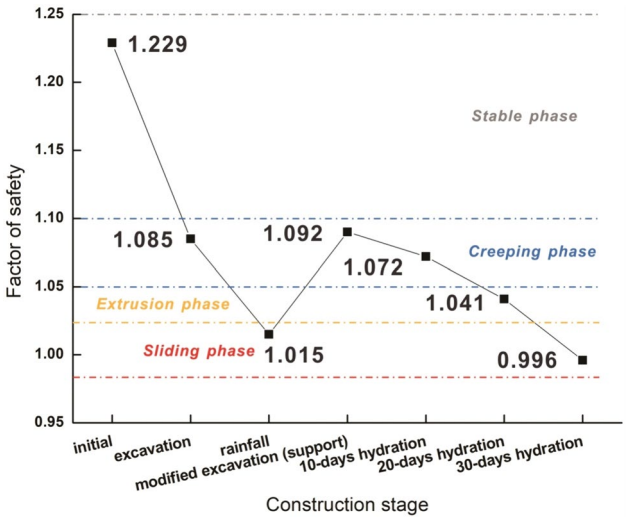

Fig.6 Factor of safety at each stage of the slope

Slope failure characteristics

Figure 7 illustrates that the slope is stable at the initial stage, with a factor of safety of 1.229. Following the initial excavation, the factor of safety decreased to 1.085, indicating the onset of the creeping stage. Deformation concentrated in the surface from the middle first-level to the lower fourth-level slope, as shown in Fig. 7(a). Additionally, a shallow sliding surface occurred from the top of the excavated slope to the slope toe, as depicted in Fig. 5(a). In the rainfall stage, the slope skipped the extrusion stage and directly entered the sliding stage, with the factor of safety reduced to 1.015. Rainfall infiltrated along the excavated slope, creating a transient saturation zone in the front and raising the groundwater level of the lower shale. Meanwhile, the rest remained unsaturated with suction pressure values increasing from bottom to top, as demonstrated in Fig. 7(b). This resulted in the loss of effective stress of the front soil mass and reduction of shale shear strength parameters, leading to traction landslide of the excavated slope and deformation of the middle and rear soil mass, as depicted in Fig. 7(c).

Following the modified excavation and support, the slope stability greatly improved, with the factor of safety rising to 1.092, approaching the stable stage. The plastic strain nephogram showed the appearance of a shallow plastic zone from the middle to the lower part of the excavated slope, located within the anchoring range of the support structure, which did not result in sliding failure.

In the hydration stage, slope stability exhibited an accelerated decreasing trend. By the 10th day of hydration, cohesion, internal friction angle, and elastic modulus of the hydration layer decreased to 82.9% (25.7 kPa),88.3% (20.3°), and 92.4% (5.27×10^5 kPa) of initial values, respectively. The slope remained in the creeping phase, with a

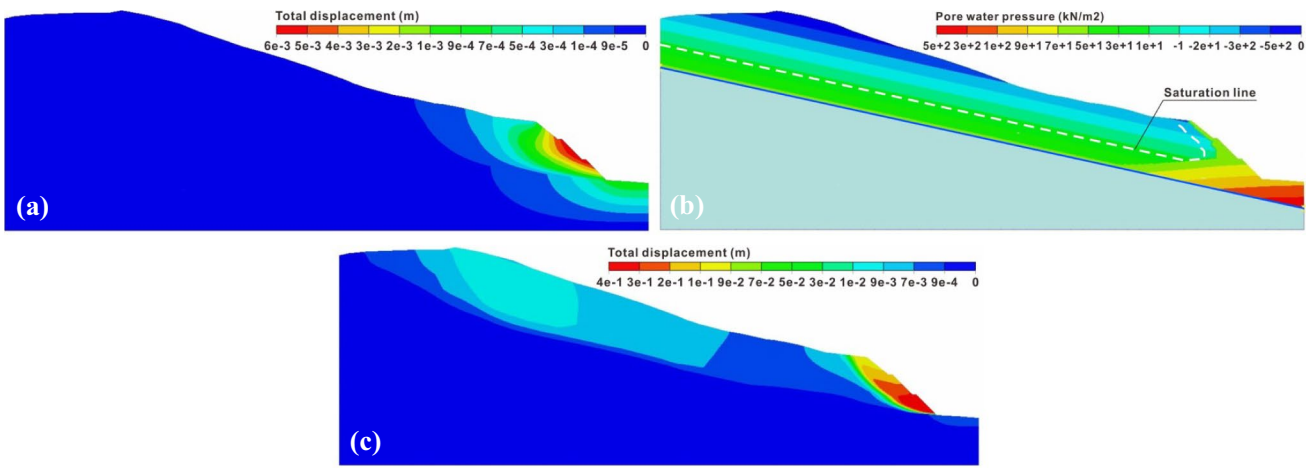

Fig.7 Deformation and seepage characteristics of slope in initial excavation and rainfall stage: (**a**) total displacement after initial excavation, (**b**) pore water pressure at 93-day of the rainfall, and (**c**) total displacement after rainfall

factor of safety of 1.072, only 1.9% lower than the previous. However, stress and deformation characteristics were significantly changed. Positive effective stress concentrated in the middle to rear of the hydration layer while surface values oscillated from positive to negative, as depicted in Fig. 8(b), indicating compression and tension occurring in deep and shallow layers. The plastic zone of the excavated slope shifted from shallow to deep, with the sliding surface bypassing the anchor rod and cutting along the exposed position of the lower shale, as shown in Fig. 5(d). This rendered the support structure ineffective and caused deformation of the first-level slope. Furthermore, due to weakened shale parameters, the middle and rear soil mass exhibited displacement exceeding 6 mm, as shown in Fig. 8(a).

On the 20th day of hydration, the factor of safety decreased to 1.041, and the slope entered the extrusion phase. Cohesion and internal friction angle reduced to 65.8% (20.4 kPa) and 76.5% (20.4°) of initial values, respectively. Additionally, elastic modulus decreased to 84.7% (4.83×10^5 kPa), significantly exacerbating progressive sliding deformation. Stress concentration from the middle to rear of the hydration layer rapidly extended downwards, forming a compressive stress band as illustrated in Fig. 8(d). Concurrently, tensile stress in the shallow layer of the excavated slope slightly increased. The stress variation, combined with expansion and increase of plastic strain in the Fig. 5(e), indicating traction sliding deformation in the excavated slope and the development of translational landslide along the hydration layer.

Compared to the 10th day of hydration, deformation range of the excavation slope greatly extended from the first level to the middle of the third level slope, with average displacement increasing from 63.5 mm to 111.8 mm, an increase of 76%. The deformation area of the middle and rear weathered layer extended downward, and displacement near the excavated slope gradually decreased, as depicted in Fig. 8(c).

At the end of the hydration, the slope exhibited instability. The factor of safety sharply dropped to 0.996, reaching sliding failure stage. The cohesion and internal friction angle reduced to the lowest, which were only 48.4% (15 kPa) and 65.2% (15°) of initial values, disrupting torque balance of weathered layer. Both compressive stress and plastic strain zone connected to front excavated slope, as shown in Figs.8(f) and 5(f). A large bedding landslide from slope toe to top had completely formed. The first-to-second-level slope displacement exceeded half a meter, consistent with the 0.6 m stagger deformation observed in the second-level platform.

By comparing the simulation results and investigation, it can be seen that the simulated sliding range is basically consistent with the sliding surface on the K158 + 430 section. The rear edges of the two are located 235 m and 239 m behind the slope shoulder, respectively, and the simulated deformation (50–80 mm) also matches the width of the tension crack (50–100 mm). In addition, the positions of the shear outlets are also close, located at the slope toe and the lower first level slope. Considering that both the simulated and actual sliding zones are carbonaceous shale below the

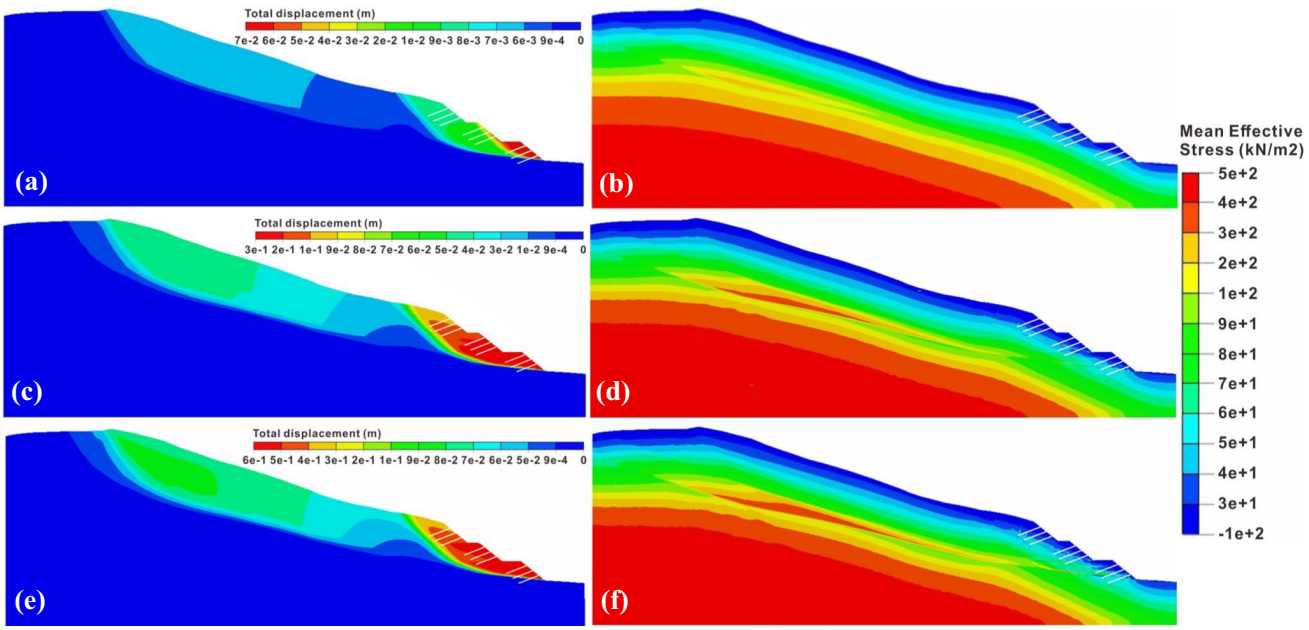

Fig.8 Stress and deformation characteristics under hydration: (**a**), (**c**), (**e**) Total displacement on the 10th, 20th, and 30th day of hydration, (**b**), (**d**), (**f**) Mean effective stress on the 10th, 20th, and 30th day of hydration

water level, it can be confirmed that the overall sliding is induced by hydration, demonstrating the simulation have reproduced the failure process.

Mechanical behavior of shale under hydration

Based on the simulation results, as hydration time increases, mechanical parameters of the lower shale linearly decrease, while sliding deformation and the rate of decline in factor of safety sharply increase. The relationship between mechanical parameters of the hydration layer and slope stability appears non-linear. To clarify the slope failure mechanism, it is necessary to analyze mechanical behavior of shale. Therefore, four measurement points every 50 m along the middle layer of the weakened shale are selected, named as Front, Middle, Middle rear, and Rear, to extract total displacement, mean effective stress, maximum shear stress, and shear strain. Figure 9 illustrates the curves of plastic strain–time, mean effective stress-time, maximum shear stress-displacement, and maximum shear stress-shear strain.

Figure 9(a) and (b) illustrate the three-stage deformation of hydrated shale. Unlike the instantaneous creep-creep stability/attenuation-accelerated creep process observed in shear tests and uniaxial compression tests (Fang et al. 2022b; Cai et al. 2019; Zhu et al. 2019a, b), the strain–time curve gradually increases. During the initial stage (1–10 days), the deformation rate remains nearly constant at zero or a low level, with no significant increase in plastic strain. In the intermediate stage (10–20 days), the deformation rate slowly increases. During the later stage (20–30 days), the deformation rate increases sharply until slope failed. The maximum shear stress exhibits a nonlinear relationship with

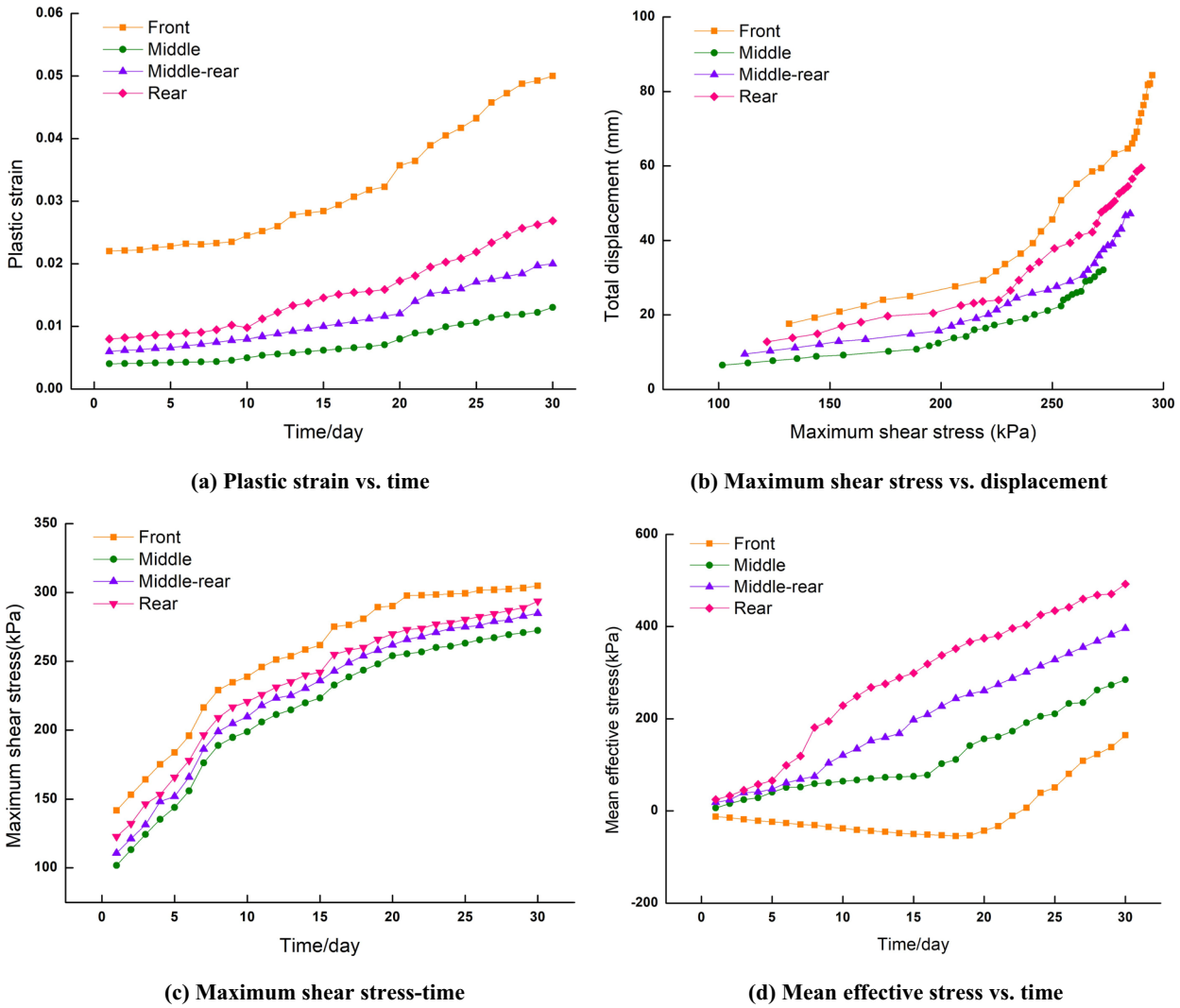

(a) Plastic strain vs. time

(b) Maximum shear stress vs. displacement

(c) Maximum shear stress-time

(d) Mean effective stress vs. time

Fig.9 Mechanical characteristics of shale under hydration. (**a**) Plastic strain vs. time (**b**) Maximum shear stress vs. displacement (**c**) Maximum shear stress-time (**d**) Mean effective stress vs. time

total displacement; as shear stress increases, displacement initially increases slowly, then accelerates before increasing sharply. This characteristic resembles the variation pattern of slope sliding failure and factor of safety at three time points (10 days, 20 days, 30 days) under hydration, indicating that water-weakening has a significant impact on slope stability.

When considering Fig. 9(c) and (d), it is evident that during the initial stage, shale exhibits anelasticity where the plastic strain lags behind the stress change. As a result of shear strength reduction, the shear stress significantly increased, with the average increment being 98 kPa at the 10th day of hydration across measuring points. Concurrently, effective stress changes at the front, rear, and middle-rear measuring points, where the front recorded tensile stress increasing from -12.5 kPa to -38.1 kPa, the data obtained at the rear and middle rear indicated compressive stress, with values increasing from 18.47 kPa and 24.69 kPa to 120.81 kPa and 228.97 kPa, respectively. However, the plastic strain remained relatively constant. Despite slight shale mechanical parameter reduction altering the slope stress state, the residual shear strength enabled the hydrated layer to remain stable, and the high elastic modulus restricted deformation. During the intermediate stage, moderate increases in plastic strain are observed. The growth rate of shear stress at each measuring point slows down, and the effective tensile/compressive stress exhibits an obviously growth, suggesting the tensile shear and compressive shear deformation are occurred at the front and middle to rear part, respectively. In the later stage, the shear stress-time curve remains almost constant, while the plastic strain continues to increase. Figure 9(b) shows that when the maximum shear stress exceeds 270 kPa, the displacement sharply rises, indicating that the hydrated shale has reached its yield limit and is rapidly damaged. The damaged soil masses at middle to rear push forward, leading to increased compressive stress and causing the front failure mode to transition from tensile shear failure to compressive shear failure.

Failure mechanism and reinforcement

Based on the slope failure characteristics and mechanical behavior of hydrated shale, it can be observed that the combined excavation and rainfall led to the initial excavated slope collapse. During the modified excavation stage, hydration accelerated the reduction of the factor of safety and increased deformation, which caused the slope damage to progress from partial to overall, eventually resulted in the alteration of slope failure mode from excavated slope collapse to deep-seated landslide and overall bedding landslide. Due to the continuous reduction of mechanical parameters, tensile and compressive shear failures first occurred in the front and rear of the lower shale. The front failure developed from front to rear, forming a deep sliding surface that caused traction sliding deformation of the modified excavated slope. The rear failure developed from the rear to the front, causing the compressive stress zone and sliding surface to connect with the front, resulting in a bedding landslide of the hydration layer. In the process of progressive failure, the sliding surface extended from front to back before connecting from back to front, thereby exhibiting a composite sliding failure characterized by traction and push landslides.

In terms of treatment effect, modified excavation and full-length bonded anchor rod support have improved the stability in the early stages of hydration. Additionally, mortar rubble protection and intercepting and drainage ditches have effectively blocked the infiltration of rainwater. However, these measures are only used to prevent the excavated slope collapse. For deep complex landslide disasters caused by hydration, the anchor rod cannot cross the sliding surface to produce an anchoring effect. Furthermore, slope protection and drainage facilities can only prevent the rise of groundwater levels and cannot curb the weakening of mechanical parameters caused by hydration. The construction and design units only treat the slope based on deformation and failure characteristics that have occurred without analyzing potential failure mechanisms comprehensively, including stress, strain, and seepage characteristics. As a result, failure of the support and protection structure is inevitable.

Given the gentle inclination and longitudinal length (320 m) of the slope stratum, the thrust generated by the bedding landslide is significant. To address this issue, the author proposes adopting a scheme of prestressed anchor cable and double row portal anti-slide pile to support the front excavated slope. The pile is poured with C30 concrete, with a length of 27 m and embedded in the bedrock of 11.6 m. The cross-sectional size is 2 m × 2 m, with a 6 m spacing and a middle connecting beam width of 2 m. The prestressed anchor cable is made of 7 steel strands with a diameter of 15.2 mm, with a single tensile strength of 1860 Mpa. The prestressed force is 700 kN, and the spacing between the anchor cables is 4 m × 4 m. The anchoring section length is 10 m, mostly embedded in landslide bed.

By simulating the slope proposed support scheme under hydration, the slope factor of safety after 30 days of hydration is 1.38, meeting China's Code for Design of Highway Subgrades' requirements for a factor of safety greater than 1.25. The compressive stress band of the hydration layer appears only at the rear, and the maximum deformation observed is 0.27 mm, indicating the support structure effective control deformation, as shown in Fig. 10(a) and (b).

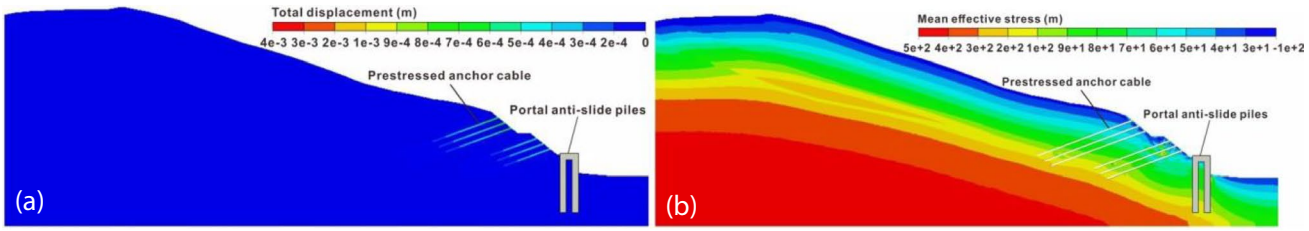

Fig.10 Stress and deformation of slope with proposed reinforcement under 30 days hydration: (**a**) total displacement, and (**b**) mean effective stress

Conclusions

(1) To analyze the impact of water weakening on slope stability, an engineering slope disturbed by excavation and rainfall was taken as an example. Through on-site investigation and geological survey, it was evident that the hydration of shale below the water level induced the overall slope instability. Based on the parameter inversion and formula calculations, the elastic modulus and shear strength parameters of hydrated shale were determined and used to simulate the gradual weakening process. The actual failure process of the slope was numerically reproduced, and the resulting simulation was compared against the on-site landslide characteristics. The slope failure mechanism under hydration was subsequently analyzed. The results indicates that the hydration accelerates the reduction of the slope stability and increases deformation, thereby causing traction and push type landslides along the front and rear of the hydrated shale layer.

(2) Unlike laboratory tests that yield instantaneous creep-creep stability/attenuation-accelerated creep processes, the plastic strain of the slope shale layer under hydration reveals a three-stage process involving initial growth weakness, medium-term accelerated growth, and late sharp increase with time. Additionally, the maximum shear stress and total displacement exhibit similar nonlinear relationships. Shale exhibits anelasticity in the early stages of hydration, and its plastic strain remains unchanged with the growth of shear and effective stress. During the middle stage, as the plastic strain gradually increases, tensile shear and compressive shear deformation occur in the front and rear of shale, respectively. In the later stage, the shale reaches its yield limit of maximum shear stress (270 kPa) and ultimately fails. Meanwhile, the damaged masses at the rear and middle compress the front, resulting in a transition of failure mode to compressive shear failure.

(3) The failure reasons of the slope protection structure in this case were analyzed. A prestressed anchor cable support scheme for hydration was proposed, and its feasibility was verified through numerical simulation. Results show that when dealing with engineering slopes containing groundwater, the rise of groundwater level caused by excavation and rainfall infiltration can cause the shift from local to overall slope damage, while the sliding range converts from shallow to deep. Comprehensive measures such as excavation, protection, surface waterproofing and drainage engineering are difficult to effectively prevent and control deep landslides caused by hydration. Additionally, the design idea that only considers the displacement characteristics of the shallow masses while ignoring deep stress, strain, and seepage characteristics has significant shortcomings.

Acknowledgements The present work was financially supported by the UK Research and Innovation (UKRI) (Grant No. EP/Y02754X/1) and the UK Engineering and Physical Sciences Research Council (EPSRC) New Investigator Award (Grant No. EP/V028723/1).

Data availability The data underpinning this publication can be accessed from Brunel University London's data repository, Brunelfigshare here under a CCBY licence: https://doi.org/10.17633/rd.brunel.26131048

Declarations

Disclosure The authors declare that they have no known competing financial interests or personal relationships that could appear to influence the work reported here.

References

Bastian VDB, Lombardo L, Ma CY, van Westen CJ, Jetten V (2021) Physically-based catchment-scale prediction of slope failure volume and geometry. Eng Geol 284:105942

Bian K, Liu J, Zhang W, Zheng X, Ni S, Liu Z (2019) Mechanical behavior and damage constitutive model of rock subjected to

water-weakening effect and uniaxial loading. Rock Mech Rock Eng 52:97–106
Bishop AW (1959) The principle of effective stress. Tecknisk Ukeblad 106(39):859–863
Cai X, Zhou Z, Liu K, Du X, Zang H (2019) Water-weakening effects on the mechanical behavior of different rock types: phenomena and mechanisms. Appl Sci 9:4450
Chen GQ, Li TB, Gao MB, Chen ZQ, Xiang TB (2013) Deformation warning and dynamic control of dangerous disaster for large underground caverns. Disaster Adv 6(S1):228–235
Chen G, Li T, Wang W, Zhu ZF, Chen ZQ (2019a) Weakening effects of the presence of water on the brittleness of hard sandstone. Bull Eng Geol Env 78:1471–1483
Chen X, Eichhubl P, Olson JE, Dewers TA (2019b) Effect of water on fracture mechanical properties of shales. J Geophys Res Solid Earth 124:2428–2444
Ewy R (2014) Shale swelling/shrinkage and water content change due to imposed suction and due to direct brine contact. Acta Geotech 9(5):869–886
Fang K, Miao MH, Tang HM, Dong A, Jia SX, An PJ, Zhang BC, Tu JM (2022a) Model test on deformation and failure behaviour of arching-type slope under excavation condition. Eng Geol 302:106628
Fang XX, Feng H, Li F, Wang H (2022b) Creep mechanical properties and constitutive model of hard brittle mud shale. Clays Clay Miner 70:307–327
Feng X, Gong B, Cheng X, Zhang H, Tang C (2022) Anisotropy and microcrack-induced failure precursor of shales under dynamic splitting. Geomat Nat Haz Risk 13:2864–2889
Fredlund DG (1998) Bringing unsaturated soil mechanics into engineering practice. The 2nd International Conference on Unsaturated Soil, Beijing, China, pp 1–51
Fredlund DG, Lim PC (1994) Matric suction and diffusive transport in centrifuge models: Discussion. Can Geotech J 32(1):178–180
Gong B (2021) Study of PLSR-BP model for stability assessment of loess slope based on particle swarm optimization. Sci Rep 11:17888
Gong B, Tang C (2017) Slope-slide simulation with discontinuous deformation and displacement analysis. Int J Geomech 17(5):E4016017
He F, Tan SC, Liu HJ (2022) Mechanism of rainfall induced landslides in Yunnan Province using multi-scale spatiotemporal analysis and remote sensing interpretation. Microprocess Microsy 90:104502
Huang D, Gu DM (2017) Influence of filling-drawdown cycles of the Three Gorges reservoir on deformation and failure behaviors of anaclinal rock slopes in the Wu Gorge. Geomorphology 295:489–500
Ishii Y, Ota K, Kuraoka S, Tsunaki R (2012) Evaluation of slope stability by finite element method using observed displacement of landslide. Landslides 9(3):335–348
Jiang Q, Cui J, Feng X, Jiang Y (2014) Application of computerized tomographic scanning to the study of water-induced weakening of mudstone. Bull Eng Geol Env 73(4):1293–1301
Kang ZY (2019) Research on the weakening mechanism of the soaked shale and corresponding permeability evolution. Master's thesis, Chongqing University, Chongqing, China
Leng YJ, Tang HM, Feng YT, Wu JY, Zheng MJ, Wu W, Luo C, Zhao SX (2022) Shale hydration and its influencing effect on water phase flowback: a case of Longmaxi formation in Weiyuan area, Sichuan Basin. J Cent South Univ(Sci Technol) 53(9):3681–3693
Li Q, Wang YM, Zhang KB, Yu H, Tao ZY (2020a) Field investigation and numerical study of a siltstone slope instability induced by excavation and rainfall. Landslides 17(6):1485–1499
Li Z, Liu SG, Fang JJ, Zhu QH, Dun Z (2020b) Multiscale laboratory study and numerical analysis of water-weakening effect on shale. Adv Mater Sci Eng 2020:5263431
Liang Z, Gong B, Tang C, Zhang Y, Ma T (2014) Displacement back analysis for a high slope of the Dagangshan hydroelectric power station based on BP neural network and particle swarm optimization. Scientific World Journal 2014:74132
Lin F, Wu LZ, Huang RQ, Zhang H (2018a) Formation and characteristics of the Xiaoba landslide in Fuquan, Guizhou, China. Landslides 15:669–681
Lin F, Wu LZ, Huang RQZ, H, (2018b) Formation and characteristics of the Xiaoba landslide in Fuquan, Guizhou, China. Landslides 15:669–681
Liu Z, Yan Z, Wang XG, Li JW, Qiu ZH (2021) Effect of the inclined pile-soil arch in a soil landslide reinforced with anti-sliding piles. Nat Hazards 106:2227–2249
Liu W, Yang K, Zhang S, Zhang ZN, Xu RJ (2022) Energy evolution and water immersion-induced weakening in sandstone roof of coal mines. Int J Coal Sci Technol 9:53
Mao HJ, Guo YT, Wang GJ (2010) Evaluation of impact of clay mineral fabrics on hydration process. Rock and Soil Mechanics 31(09):2723–2728
Meng QX, Qian K, Zhong L, Gu JJ, Li Y, Fan KF, Yan L (2020) Numerical analysis of slope stability under reservoir water level fluctuations using a FEM-LEM-combined method. Geofluids 2020:6683311
Moazeni-Noghondar S, Golkarian A, Azari M, Behnam AL (2021) Study on soil water retention and infiltration rate: a case study in eastern Iran. Environ Earth Sci 80:474
Nguyen VU (1984) Back calculations of slope failures by the secant method. Geotechnique 34(3):423–427
Oh S, Lu N (2015) Slope stability analysis under unsaturated conditions: Case studies of rainfall-induced failure of cut slopes. Eng Geol 184:96–103
Panday S, Dong J (2021) Topographical features of rainfall-triggered landslides in Mon State, Myanmar, August 2019: spatial distribution heterogeneity and uncommon large relative heights. Landslides 18:3875–3889
Parker JC, Kool JB, van Genuchten MT (1985) Determining soil hydraulic properties from one-step outflow experiments by parameter estimation: II experimental studies. Soil Sci Soc Am J 49:1354–1359
Peng JB, Fan ZJ, Wu D, Huang QB, Wang QY, Zhuang JQ, Che WY (2019) Landslides triggered by excavation in the loess plateau of China: A case study of Middle Pleistocene loess slopes. J Asian Earth Sci 171:246–258
Qiu X, Li J, Jiang HB, Ou J, Ma JQ (2022) Evolution of the transient saturated zone and stability analysis of slopes under rainfall conditions. KSCE J Civ Eng 26:1618–1631
Robert DJ (2017) A modified Mohr-Coulomb model to simulate the behavior of pipelines in unsaturated soils. Comput Geotech 91:146–160
Shi G, Yang X, Chen W, Chen H, Zhang JC, Tao ZG (2021) Characteristics of failure area and failure mechanism of a landslide in Yingjiang County, Yunnan, China. Landslides 18:721–735
Shinoda M, Miyata Y, Kurokawa U, Kondo K (2019) Regional landslide susceptibility following the 2016 Kumamoto earthquake using back-calculated geomaterial strength parameters. Landslides 16(8):1497–1516
Tao T, Shi W, Liang F, Wang XM (2022) Failure mechanism and evolution of the Jinhaihu landslide in Bijie City, China, on January 3, 2022. Landslides 19:2727–2736
Tong FK (2018) The research on structure and performance of rubber powder modified asphalt pavement of Shangdeng expressway. Master's thesis, Changsha University of Technology, Changsha, China
Wang QE (2012) Study on structure and hydro-mechanical properties of sliding zone soil in Huangtupo landslide. Doctoral dissertation, China University of Geosciences (Wuhan), Wuhan, China

Wang P (2015) Mechanics research on creep buckling of the shale hydration damage. Doctoral dissertation, Northwestern Polytechnical University, Xi'an, China

Wang Y, Gong B, Zhang Y, Yang X, Tang C (2022) Progressive fracture behavior and acoustic emission release of CJBs affected by joint distance ratio. Mathematics 10(21):4149

Wang H, Wang XD, Pan J (2017) A case study of super-high cut slope I: simulation and analysis of instability mechanism of slopes. Chin J Rock Mech Eng 4:125–135

Wong LNY, Maruvanchery V, Liu G (2016) Water effects on rock strength and stiffness degradation. Acta Geotech 11:713–737

Xu YB, Wei CF, Chen H, Luan MT (2008) A model of soil-water characteristics for unsaturated geotechnical materials under arbitrary drying-wetting path. Chin J Rock Mech Eng 198(5):1046–1052

Xu J, Li H, Wang H, Tang L (2023) Experimental study on 3D internal penny-shaped crack propagation in brittle materials under uniaxial compression. Deep Underground Sci Eng 2(1):37–51

Yang H, Yang T, Zhang S, Zhao F, Hu K, Jiang Y (2020a) Rainfall-induced landslides and debris flows in Mengdong Town, Yunnan Province, China. Landslides 17:931–941

Yang F, Zhou H, Zhang C, Lu J, Lu X, Geng Y (2020b) An analysis method for evaluating the safety of pressure water conveyance tunnel in argillaceous sandstone under water-weakening conditions. Tunn Undergr Space Technol 97:103264

Yang K, Yan Q, Zhang C, Wu W, Wan F (2021) Study on mechanical properties and damage evolution of carbonaceous shale under triaxial compression with acoustic emission. Int J Damage Mech 30(6):899–922

Yang J, Fan P, Wang M, Li J, Dong L (2023) Experimental study on the irreversible displacement evolution and energy dissipation characteristics of disturbance instability of regular joints. Deep Underground Sci Eng 2(1):20–26

Yu X, Gong B, Tang CA (2021) Study of the slope deformation characteristics and landslide mechanisms under alternating excavation and rainfall disturbance. Bull Eng Geol Env 80:7171–7191

Zhang JY, Wan LP, Pan HY, Li JL, Luo ZS, Deng HF (2017) Long-term stability of bank slope considering characteristics of water–rock interaction. Chinese J Geotech Eng 39(10):1851–1858

Zhang JM, Zhou Z, Lin F, Yang QG, luo Y, (2021) Failure mechanism of a slow-moving landslide on September 27, 2020, in Chang Nong Village, Guangxi, China. Landslides 18:2575–2592

Zhao L, Li D, Tan HC, X., Zuo S, (2019) Characteristics of failure area and failure mechanism of a bedding rockslide in Libo County, Guizhou, China. Landslides 16:1367–1374

Zhao Z, Li W, Ma J, Yang M, Kou H, He Y, Zheng S, Dong A (2022a) Saturated water-weakening effects on the compressive behavior of thermally damaged granite. Fatigue Fract Eng Mater Struct 45(8):2329–2343

Zhao ZH, Jin ZH, Guo JC, Chen MT, Lu C (2022b) Study on softening constitutive model of deep shale under hydration. Chin J Rock Mech Eng 41:3189–3197

Zhu SN, Yin YP, Li B (2019a) Shear creep behavior of soft interlayer in Permian carbonaceous shale. Rock and Soil Mechanics 9:4450

Zhu S, Yin Y, Li B et al (2019b) Shear creep characteristics of weak carbonaceous shale in thick layered Permian limestone, southwestern China. J Earth Syst Sci 128:28

Zhu YJ, He N, Zhong W, Kong JM (2020) Physical simulation study of deformation and failure accumulation layer slope caused by intermittent rainfall. Rock Soil Mech 41(12):4035–4044

Zhu J, Deng JH, Ma YJ, Ronald YSP, Zhang ZH (2022) Experimental study on the competing effects of strain rate and water weakening on compressive strength of saturated rocks. Eng Geol 310:106873